High-Density Periodic Arrays of Self-Aligned Subwavelength Nanopyramids for Surface-Enhanced Raman Spectroscopy

Mingliang Jin,[†] Vishnu Pully,[‡] Cees Otto,[‡] Albert van den Berg,[†] and Edwin T. Carlen*[,†]

BIOS Lab on a Chip Group, Medical Cell BioPhysics Group, MESA$^+$ Institute for Nanotechnology, and MIRA Institute for Biomedical Technology and Technical Medicine, University of Twente, Enschede, The Netherlands

Received: July 6, 2010; Revised Manuscript Received: November 15, 2010

Novel nanotextured surfaces are presented with periodically self-aligned subwavelength nanogroove and nanopyramid structures with precisely defined pitch λ_g that are closely packed with 2 nm separation gaps over large areas and form high-density arrays of hot-spot scattering sites ideally suited for surface-enhanced Raman scattering (SERS) and Raman spectroscopy. The simple self-aligning fabrication technique requires only a single lithography step and wet anisotropic etching. Measured average Raman enhancement factors of $G \approx 10^6$ from rhodamine 6G (R6G) on patterned Au surfaces with $\lambda_g = 200$ nm are consistent with numerical calculations. The nanostructured surfaces can be scaled to smaller dimensions, which results in increased enhancement as well as increased hot-spot spatial density.

Introduction

Since the discovery of SERS on noble metal surfaces,[1−3] a new era for Raman spectroscopy has emerged for molecular identification in aqueous solutions at low sample concentrations, which provides a unique capability for the label-free detection and identification of a variety of different analytes. Since the first SERS report, Raman scattering enhancements spanning several orders of magnitude, compared to normal Raman scattering, down to the single-molecule level have been reported.[4−8] The mechanisms responsible for SERS on metal nanostructured surfaces include electromagnetic field enhancements, molecular resonances and charge-transfer transitions;[9] however, the electromagnetic enhancement is considered the dominant process.[10] The electromagnetic field enhancement is electrodynamically generated when surface plasmons of the metal nanostructures couple with incident excitation photons. Metal nanostructures with sharp points and rod-shaped nanoparticles produce locally enhanced electromagnetic fields due to the lightning-rod effect; however, the largest electromagnetic enhancements arise from the plasmon interactions of at least two adjacent nanostructures (dimers) in the form of spatially localized surface plasmon resonances that lead to large electromagnetic field enhancements of the excitation field near the metal surface and enabled the detection of SERS from single molecules.[4−8] The small separation gaps between dimers are typically referred to as SERS *hot-spots* and have motivated the field of hot-spot engineering in an attempt to optimize the SERS figure of merit, which includes large enhancements, reproducibility, and dynamic range.

Despite the steady progress achieved over the last three decades, SERS substrates still have figure of merit limitations, which fundamentally depend on the ability to manufacture large area nanostructure arrays with well-controlled dimensions, geometry, and polarization alignment, and most importantly hot-spot dimensions less than ∼5 nm; all contribute to the enhancement of the Raman scattering cross-section of molecules adsorbed on the metal surface. Many different techniques have been reported to fabricate functional metallic SERS-active substrates. Colloidal suspensions of metal nanoparticles of various shapes and sizes have been reported[10−16] and were used to realize single molecule Raman spectra[5−8] where large enhancements were attributed to nanoparticle dimers with ∼1−2 nm separations.[17] Colloidal nanoparticle suspensions are attractive due to their preparation simplicity; however, they typically have poor enhancement reproducibility, which is attributed to many factors including their random composition and the lack of precise control of dimensions, dimer separation spacing, and excitation polarization alignment.

SERS-active solid-support substrates have been reported extensively over the last three decades. Low-cost nonlithographic methods have been reported, such as electrochemically roughened surfaces, self-assembled templated colloidal films,[18,19] nanoporous templated surfaces,[20,21] shadow masked deposited metal (nanosphere lithography) island films,[22] and voids,[23] and nanocasted spherical void surfaces;[24] however, forming small and uniform separation gaps is difficult. Lithographically patterned SERS substrates still constitute one of the most promising manufacturing methods to form large arrays of reproducible hot-spots due to their readily available, and highly advanced, patterning techniques. Patterning thin metal layers by using a variety of different nanolithography techniques, such as electron-beam patterning, focused ion beam milling, holography, and nanoimprinting, have been reported to realize SERS-active surfaces in a large variety configurations, including metal discs of many shapes, sizes and gap-separations,[25−28] nanohole arrays,[29] bowtie antenna nanostructures,[30] arrays of nanoslits,[31] and gratings. Surface templates fabricated by the anisotropic etching of crystalline silicon to form nanostructured surfaces with well-controlled dimensions and sharp edges have been reported, such as the commercially available inverted pyramidal pit arrays (Klarite 302, Renishaw Diagnostics, Ltd.),[32] inverted nanopyramidal pits,[33] and nanopyramids with sharp tips.[34]

Grating structures are an important class of SERS-active substrate and have been reported for over three decades,[35−45] due to well-established manufacturing and analysis methods.

* To whom correspondence should be addressed.
[†] BIOS Lab on a Chip Group.
[‡] Medical Cell BioPhysics Group, MESA$^+$ Institute for Nanotechnology, and MIRA Institute for Biomedical Technology and Technical Medicine.

10.1021/jp106245a
Published on Web 12/02/2010

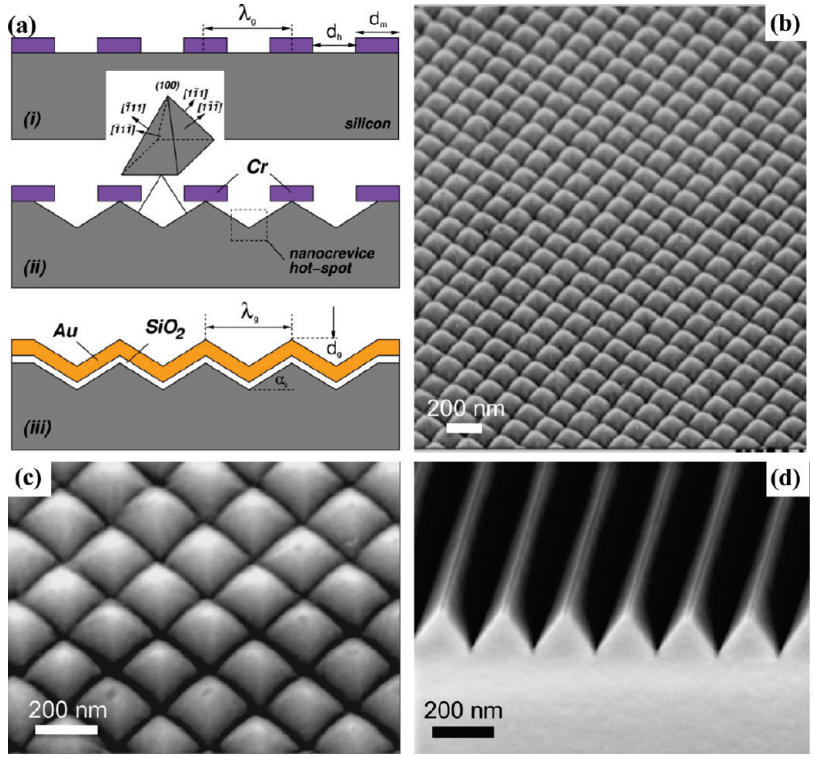

Figure 1. Nanotextured surfaces. (a) Fabrication overview. Inset: Nanopyramid geometry. (b−d) High-resolution scanning electron microscopy images of subwavelength nanotextured silicon surfaces: (b, c) two-dimensional nanopyramid surfaces and (d) one-dimensional nanograting surface.

The early research on the optical properties of metallic gratings typically reported grating pitches near the excitation wavelength[35−40] and later reports, experimental and theoretical, developed the basic understanding of the geometry-dependent optical properties of zero-mode subwavelength nanogratings;[41−45] all subwavelength nanograting structures exhibit large electromagnetic field enhancements near the base of the nanograting structure, which increases as the pitch decreases.

There remains strong demand for SERS-active substrates having a large density of uniform hot-spot scattering sites that possess large Raman enhancements with high reproducibility and stability. We present two types of subwavelength surfaces: nanogratings and nanopyramid arrays that are fabricated with a new self-aligned silicon template method that results in ultraprecise nanoscale pitch λ_g, and most importantly, highly uniform and sharp nanoscale v-groove crevices consisting of gaps with controlled 2 nm spacing. The advantage of this approach is that the gap spacing between closely packed nanopyramid neighbors is not constrained by lithographic patterning limitations, but rather realized with the extremely precise etching of certain crystalline planes of silicon, and therefore, results in high density arrays of closely packed nanopyramids and nanogratings forming uniform SERS hot-spots.

Experimental Methods

Fabrication. Figure 1a shows the fabrication overview. First, chrome nanodisk arrays were created with a lift-off process. A periodic array (40 × 40 μm^2) of nanoholes was patterned in a spin-coated electron-sensitive photoresist layer on a conventional silicon (100) wafer using electron-beam lithography. A 100 nm polymethyl methacrylate (PMMA) electron-sensitive photoresist was spin-coated on a silicon substrate and exposed to a 130 pA electron beam with the area dose in the range of 90−120 $\mu As\ cm^{-2}$ (FEI Sirion UHR-SEM). Nanohole arrays were generated in the PMMA layer following development in 1:3 methyl isobutyl ketone/isopropanol (MIBK/IPA) solution for 30 s, followed by immersion in isopropyl alcohol. A 17 nm Cr layer was electron-beam evaporated onto the patterned PMMA layer and subsequently immersed into an ultrasonic acetone bath for 2 min to remove the PMMA layer. Prior to silicon etching, the native oxide on the exposed silicon regions was removed by immersing in 1% hydrofluoric acid solution for 1 min and subsequently rinsed with deionized H_2O. The silicon was etched in a 20% KOH solution at 55 °C with stirring for 20 s and rinsed with deionized H_2O. The different crystal planes etch anisotropically by hydroxide ions in an alkaline solution where (111) planes have the lowest etch rate and (100) and (110) planes both have higher etch rates.[46] The surfaces were then cleaned in piranha solution (H_2SO_4:H_2O_2 = 3:1) for 15 min, rinsed with deionized H_2O, and dried with N_2. Prior to metallization a 10 nm oxidation layer was formed on (111) silicon by dry oxidation at 950 °C. A (111) silicon sample was used to verify the oxide thickness. The gold layer ($t_{Au} \approx 70$ nm) was sputtered-coated (DC source) from a high-purity Au target in Ar plasma (1 nm s^{-1}). An optically thick metal film prevents radiation damping into the substrate supporting the metal film.

AFM Imaging. The tapping mode atomic force images were recorded with a Dimension V SPM System (Veeco, USA) and ultra-sharp silicon tips with 2 nm average tip diameters (SSH, Nanoandmore, GmbH).

FDTD Simulation. 2D FDTD calculations performed with Fullwave (RSoft, Inc.). Perfectly matched layer boundary conditions have been used at the grid edges, to eliminate reflections, at $x = \pm 3\lambda_g/2$ and $z = \{0, 5d_g\}$ with 0.3 nm grid spacing. The complex frequency-dependent dielectric function $\varepsilon_m(\omega)$ of Au is represented by the Brendel−Borman model that is included in the simulation code. All simulations were checked for convergence.

Confocal Raman Instrumentation. Two confocal Raman microscopy systems have been used for measurements. The first Raman microscope records spectral information from 646 to 849 nm in 1600 pixels on a TE-cooled electron-multiplied charged coupled device (Newton DU-970N, Andor Technology, Belfast, Northern Ireland). A cw krypton ion laser (Coherent, Innova 90K, Santa Clara, CA; $\lambda_0 = 647.1$ nm) was used as a single excitation source with a power of 135 μW. A Nikon M-Plan 40× SLWD bright field objective (NA: 0.40, WD: 14.9 mm) was used to focus (diffraction limited with approximately 400 nm diameter) the laser on the nanostructured surface at normal incidence and to collect the Raman scattered light from the sample surface. The second confocal Raman microscope system (alpha300R, Witech GmbH) consists of a TE-cooled charge coupled device (DU401-BR-DD, Andor Technology, Belfast, Northern Ireland), diode laser (Topica Photonics XTRA high power single frequency diode laser; 150 mW; $\lambda_0 = 785$ nm), NIR UHTS300 spectrometer (f/4 300 mm FL; grating: 600 L mm^{-1}), and a Nikon CFI Achromat oil immersion 100× objective (NA: 1.25; CGC; WD: 0.18 mm) with a similar diffraction limited excitation region.

Raman Measurements. All measurements have been performed in aqueous solution. All samples of varying concentrations were diluted from a stock solution of 10^{-2} M R6G ([9-(2-ethoxycarbonylphenyl)-6-(ethylamino)-2,7-dimethylxanthen-3-ylidene]ethylazanium chloride, Aldrich, R4127) that was prepared by dissolving 4.8 mg of R6G in deionized H_2O. All data were smoothed with an FFT smoothing algorithm with $n = 3$ data points.

R6G Adsorption. The 10^{-5} L volume of sample spreads over the entire substrate surface (area: 50 mm^2) when covered with the glass slide (25 × 25 mm^2, Menzel-Glaser), and therefore, the sample approximately conforms to an area of 50 mm^2 and 0.2 mm height. Since R6G adsorbs strongly to glass surfaces, we estimate that half of the available R6G molecules are available to adsorb to the Au surface. The 10^{-7} M sample with 10^{-5} L volume results in $0.5 \times (10^{-7}$ mol L$^{-1}) \times (10^{-5}$ L) $\times (6.02 \times 10^{23}$ mol$^{-1}) \approx 3 \times 10^{11}$ molecules. As an upper limit estimation of the number of R6G molecules adsorbed on the surface, we assume that all molecules in the half-space adsorb uniformly onto the entire Au surface, thus resulting in a surface coverage density of $(3 \times 10^{11}$ molecules)/$(50 \times 10^{-6}$ m$^2) \approx 6 \times 10^{15}$ molecules m^{-2}. Assuming a circular 400 nm diameter diffraction limited spot size of the confocal microscope results in an upper limit of $(1.3 \times 10^{-13}$ m$^2) \times (6 \times 10^{15}$ molecules m$^{-2}) \approx 756$ molecules in the excitation region, which is reasonable since the lateral dimensions are much larger than the vertical dimension (>20×). Considering R6G molecules adsorbed only in the polarization direction of the hot-spot regions results in an upper limit of about 24 molecules in the excitation region.

Results and Discussion

The nanopyramid arrays have been fabricated with a new self-aligned silicon template method based on conventional top-down microfabrication technology, including a single lithography step, wet anisotropic silicon etching, oxidation, and metal deposition (Figure 1a). An important aspect of this approach is that the nanocrevice hot-spots are not formed by the lithography step, but rather the silicon etching step. Furthermore, precise alignment of the nanohole array is not required due to the regularity of the single crystal silicon, which facilitates the self-aligned formation of the two-dimensional nanopyramids (Figure 1c) that are spontaneously formed with precisely controlled λ_g and self-aligned into uniform nanopyramid arrays (Figure 1b). The surface pitch can be tuned to different dimensions by changing the mask d_m and hole d_h dimensions. The surface pattern pitch and depth are ideally linked by the silicon crystal arrangement with $d_g \approx (\lambda_g/2) \tan \alpha_g$, where $\alpha_g \approx 54.7°$ for (100) silicon. Although we use electron-beam lithography to pattern the submicrometer feature sizes, other well-established and cost-effective nanolithography methods, such as deep-UV lithography or laser interference lithography, can be used as well. Other materials and orientations can also be considered using this general technique. The high-resolution scanning electron microscopy image of a representative patterned two-dimensional surface at an increased zoom demonstrates the effectiveness of this simple method to produce highly regular and reproducible nanotextured surfaces (Figure 1c).

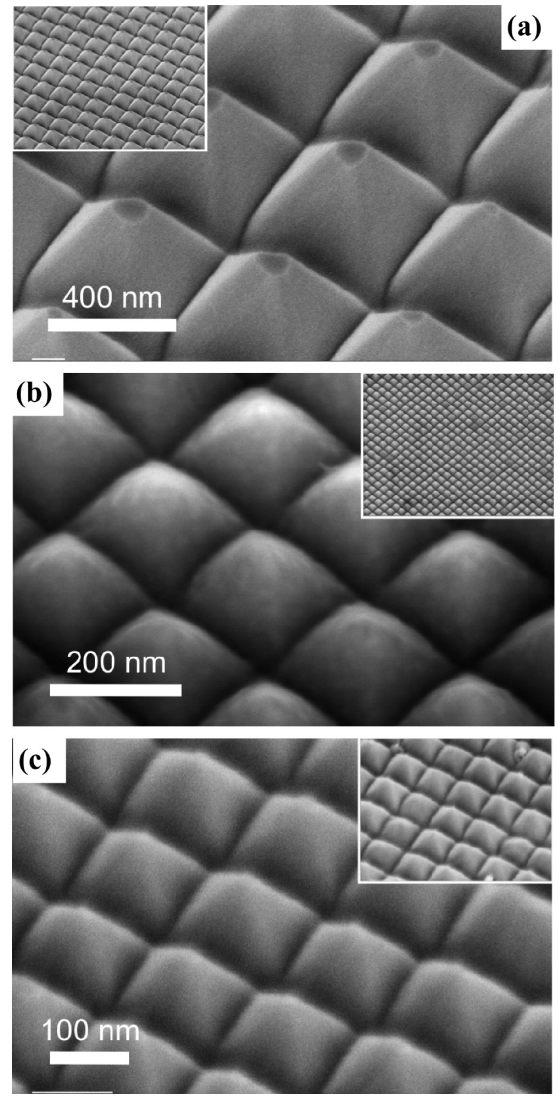

Figure 2. High-resolution scanning electron microscopy images of nanopyramid surfaces with tunable pitch λ_g: (a) 500, (b) 200, and (c) 150 nm.

One-dimensional nanogroove surfaces, fabricated with a similar method,[47] have been realized (Figure 1d). Figure 2 shows examples of fabricated subwavelength surfaces with pitches ranging from $\lambda_g = 500$ nm down to about 150 nm, which is the practical pattern definition limit of our electron-beam patterning system that is capable of resolving a minimum d_m and d_h of around 80 nm, where $\lambda_g \approx d_m + d_h$ (Figure 1a).

An important distinction between the subwavelength surfaces presented here and the inverted pyramid structures is that our

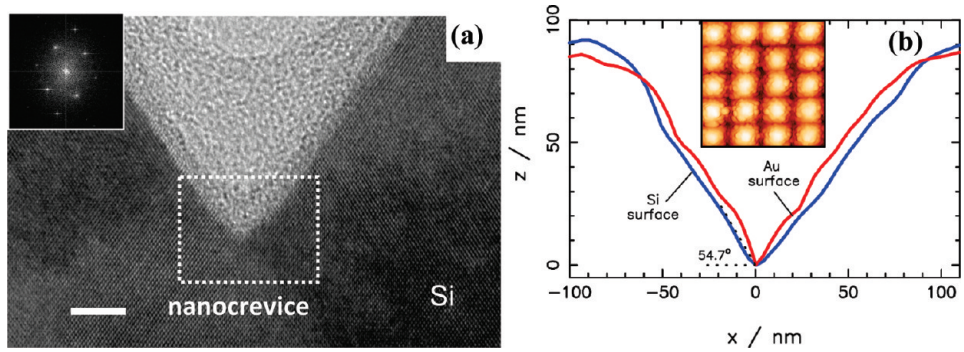

Figure 3. High-resolution microscopy images of the nanocrevice. (a) High-resolution transmission electron microscopy image of the nanocrevice region. Inset: Diffraction image silicon crystal [110] direction. Scale bar: 5 nm. (b) Atomic force microscopy profiles of the nanocrevice etched in the silicon surface (blue) and following Au deposition (red). Inset: Au-coated surface.

new surfaces can be scaled to much smaller lateral dimensions, which results in increased Raman enhancements as well as hot-spot spatial density.

Figure 3 shows high-resolution microscopy images of the nanocrevice dimensions. A high-resolution transmission electron microscopy image, prior to Au coating, of a representative silicon nanocrevice hot-spot with ~2 nm separation gap is shown in Figure 3a. Figure 3b shows atomic force microscopy profiles of a typical nanopyramid array surface before, and after, metal deposition. The surface roughness of the Au layer is evident. For arrays with pitch $\lambda_g = 150$ nm and larger, the crevice shape is not significantly altered for $t_{Au} = 70$ nm (Figure 3b) and in some cases the nanocrevice gap is reduced, which will result in increased field enhancements at the base of the crevice.

For smaller λ_g, the metal layer deposition procedure requires careful control to ensure that the crevice shape is maintained or improved with smaller gap distances. We are currently studying the effects of varying degrees of surface roughness with respect to electromagnetic field enhancements, which is important for scaling to smaller dimensions. Methods are available to reduce the Au surface roughness, such as epitaxially smooth metal deposition or chemical metal polishing.

The fabrication method presented here differs from that of other silicon template methods, such as the inverted pyramids,[18] in two important ways. First, the pitch of our nanopyramids of the arrays is self-aligned by the silicon crystal and does not require feature sizes or alignment tolerances below the pitch dimension, such as with the photolithographically defined inverted pyramids and metal discs, which is very important for realizing spatially dense arrays of hot-spots, especially for use in miniaturized lab-on-a-chip systems where micrometer-scale sample analysis chambers and nanoliter volumes are commonly used. The spatial density of the new substrates is ~5 hot-spots μm^{-1} (for $\lambda_g = 200$ nm), which is 25× greater than the Klarite substrates[18] and 2× greater that the recently reported subwavelength gratings.[45] Scaling the pitch smaller than $\lambda_g = 50$ (20 hot-spots μm^{-1}) nm results in 100× greater hot-spot density than the Klarite substrates. The second important difference is the geometry of the enhancement region, which will be discussed in the next section.

Since the report of Wood[35] describing reflection anamolies from patterned metallic surfaces, a significant amount of insight has been gained about the optical properties of metals and the excitation of surface plasmon resonance.[39] Periodically roughened surfaces facilitate the generation of surface plasmon polaritons (SPP) excitation such that the momentum of photons in the dielectric is increased by the in-plane periodicity to phase-match to the SPP. When the nanostructure periodicity is smaller than the excitation wavelength, the diffraction is zero-mode; however, an evanescent field is generated with a decay length proportional to the period of the grating that results in localized electromagnetic field enhancements near the metal surface.[44] Calculated electromagnetic field enhancements $g \approx 80$ in nanocrevices, where $g(x,z,w) \equiv |\mathbf{E}_{tot}(x,z,w)/\mathbf{E}_0(x,z,w)|$ and $\mathbf{E}_{tot}(x,z,w)$ is the total electric field and $\mathbf{E}_0(x,z,w)$ is the electric field of the incident excitation, between closely spaced 30 nm diameter silver half-cylinders in contact with a vacuum dielectric have been reported.[41] Subwavelength periodic patterned surfaces with Gaussian profiles have been shown to form standing wave SPP in narrow crevices with large localized electromagnetic field enhancements near the base of the crevice.[39,42] More recently, Xuegong et al.[45] reported subwavelength gratings where the nanocrevice is formed by refilling the grating trench. In all reported subwavelength grating or patterned surfaces, large localized electromagnetic field enhancements were reported near the base of the nanocrevices due to strong coupling between surface charges from the opposing sides of the nearest-neighbor structures. The electromagnetic field enhancement results in a Raman scattering enhancement that can be approximated as $G \approx g^4$.[10] Nanopyramid surface cross sections with smooth Au layers have been modeled using two-dimensional finite difference time domain (FDTD) calculations to determine the total electric $\mathbf{E}_{tot}(x,z)$, and magnetic $\mathbf{H}_y(x,z)$ field distributions near the metal surface of the fabricated structures. The excitation source is a normally incident plane wave with transverse-magnetic polarization where the magnetic field intensity $\mathbf{H}_y$ points along the length of the cavity. The dielectric region is water with a relative permittivity $\varepsilon_d = 1.77$. It should be noted that the electromagnetic field enhancement is dependent on the excitation polarization due to the rectangular geometry involved, similar to the polarization-dependent enhancement nanoparticle dimers.[17] Figure 4a shows the Raman enhancement as a function of excitation wavelength with a maximum $G \approx 10^6$ located in the nanocrevice at an excitation wavelength of 740 nm (1.7 eV). Similar to previous reports,[41,42] the largest electromagnetic enhancement is localized at the base of the nanocrevice due to strong charge coupling between adjacent surfaces of nearest neighbor nanostructures with small separation distances. Although the calculated enhancements are large, they are smaller than previously reported[41] due to the larger entry angle $2\gamma_g$. From a surface accessibility perspective, a large entry angle is preferred, which makes the hot-spots more accessible for molecular adsorption compared to narrow and deep cavity structures. It is interesting to note that the enhancement region of the subwavelength nanopyramid and nanogroove structures

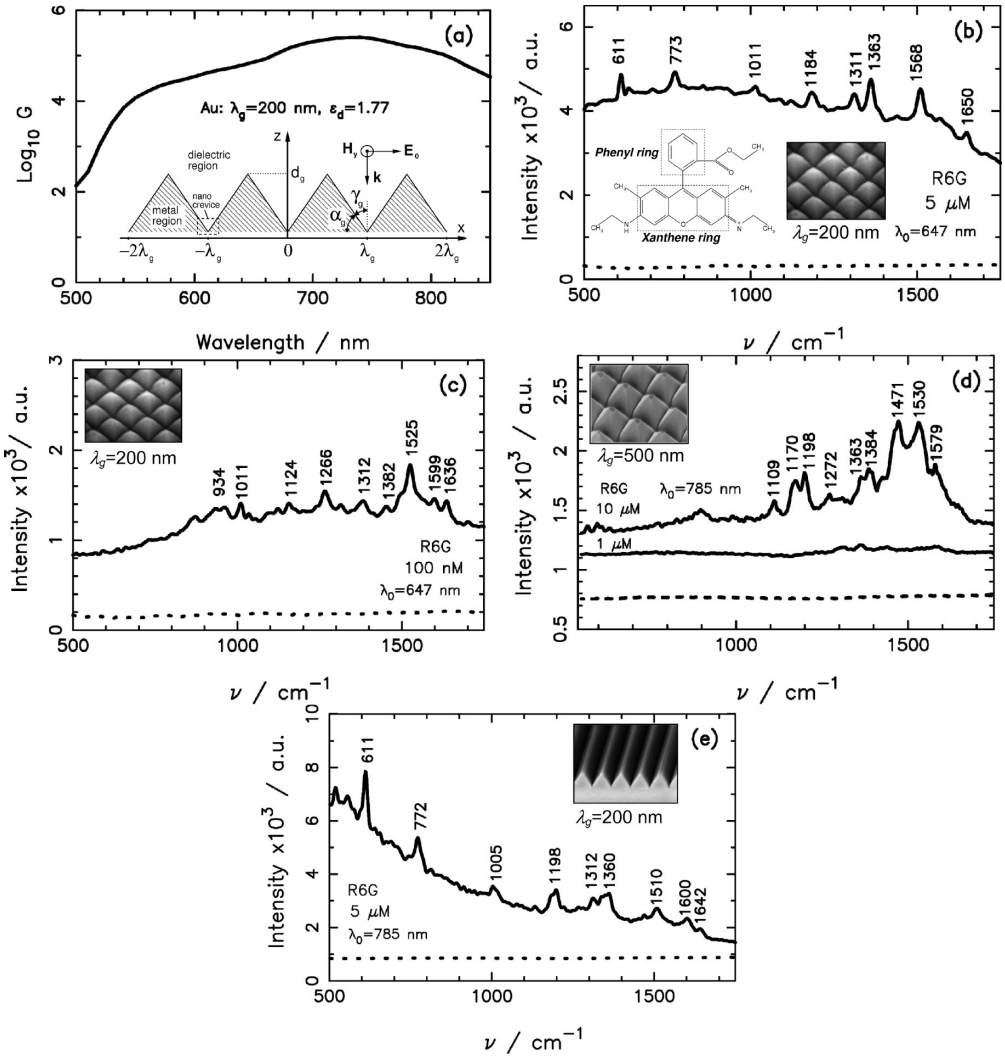

Figure 4. Calculated and measured results from nanopyramid (NP) and nanogroove (NG) surfaces. (a) 2D steady-state FDTD simulation results of Raman enhancement of a triangular cross-section (inset: surface cross-section). (b−d) Raman measurements of R6G adsorbed on flat (dotted) and NP (solid) surfaces: (b) $\lambda_g = 200$ nm and solution concentration $[C_{SERS}] = 5 \times 10^{-6}$ M; (c) $\lambda_g = 200$ nm and $[C_{SERS}] = 10^{-7}$ M; and (d) $\lambda_g = 500$ nm and $[C_{SERS}] = 10^{-6}$ M and 10×10^{-6} M. (e) Raman spectra of R6G adsorbed on NG surfaces with $[C_{SERS}] = 5 \times 10^{-6}$ M.

shows shallow v-groove structures that are very different than the Klarite inverted nanopyramid enhancement region, which has four walls leading the base of the inverted structure and results in a very different enhancement mechanism and electromagnetic field distribution.[43]

Raman spectra of physically adsorbed R6G in aqueous deionized H_2O solutions on flat and patterned nanopyramid surfaces coated with Au have been measured. Although SERS of R6G on Ag surfaces have been previously reported,[4,5,48,49] we used Au surfaces due to its chemical stability. A 10^{-5} L aliquot of each solution was placed in the center of the nanopyramid surface and immediately covered with a glass slide. Each sample was incubated for 15 min at room temperature prior to a measurement. The sample was then placed under the objective of the previously described confocal Raman microscope[50] and horizontal nanocrevices were aligned perpendicular to the excitation polarization. The acquisition time for the $\lambda_0 =$ 647 nm measurements is 30 and 10 s for the $\lambda_0 = 785$ nm measurements. Parts b and c of Figure 4 show representative measurements of R6G diluted in deionized H_2O solutions of varying concentrations on flat and nanopyramid Au surfaces excited at $\lambda_0 = 647$ nm. For reference, the molecular structure of R6G is shown in the inset of Figure 4b. Figure 4b shows Raman spectra for a 5×10^{-6} M R6G sample solution; the lower trace shows the measured sample response from a flat Au surface, which consists of the deposited Au film on a flat SiO_2/Si surface using identical measurement conditions. The measured spectral characteristics of R6G on the nanopyramid surfaces include 611, 773, 1011, 1184, 1311, 1363, 1568, and 1650 cm^{-1}. The 611, 773, and 1184 cm^{-1} modes are associated with C−C−C ring in-plane, out-of-plane bending, and C−C stretching vibrations, respectively, and the 1363, 1568, and 1650 cm^{-1} modes are associated with aromatic C−C stretching vibrations;[4] however, the 1650 cm^{-1} mode is reported to have contributions from C−H bending modes of the xanthene ring and the 1011 cm^{-1} mode is associated with the phenyl ring and $COOC_2H_5$ side groups.[51] The measured vibrational spectra compare well with previous reports with the exception of the 1011 cm^{-1} mode.[4,48]

It should be noted that most previous studies were conducted under surface-enhanced resonance Raman conditions with an excitation wavelength near the peak absorption wavelength of R6G (~532 nm). Raman spectra for a 10^{-7} M R6G concentration in deionized H_2O solution (Figure 4c) include the 934, 1011, 1124, 1266, 1312, 1382, 1525, 1599, and 1636 cm^{-1} modes, where all modes have been previously reported[4,7,48] except for the 1011 and 1525 cm^{-1} modes; the 1525 cm^{-1} mode has not been previously reported under SERS or resonant SERS

conditions and is associated with vibration of the xanthene ring and NHC_2H_5 end groups.[51] The 1636 cm^{-1} mode has not been previously assigned and is likely related to the 1650 cm^{-1} xanthene ring mode. All measurements are accompanied by a broadband *white* continuum under the Raman lines as previously reported, which has been explained as continuous scattering from the underlying metal;[48,52] however, the flat metal surfaces do not exhibit this behavior. Since each measurement was performed with a known sample volume, we estimate an upper limit of ~760 R6G molecules adsorbed on the nanopyramid surface in the confocal imaging area. It should be noted that the electromagnetic enhancement occurs only for the field polarization perpendicular to the length of the cavity, and therefore, a much smaller region of the total excitation region provides the large electromagnetic enhancement, and hence, the measured response is due to a small number of molecules. A more precise assessment of the number of molecules represented in the 10^{-7} M measurement (Figure 4c) is not possible with the current measurement system since the exact location of the active region of the crevice is not known; however, the measured spectra of the 10^{-7} M R6G concentration is associated with just a few R6G molecules in deionized H_2O. Figure 4d shows R6G spectra from a nanopyramid surface with $\lambda_g = 500$ nm and excitation $\lambda_0 = 785$ nm. The 500 nm pitch nanopyramid arrays have lower enhancements at the excitation wavelengths used here as evidenced by the requirement for larger R6G concentrations (10^{-5} M), which is consistent with previous reports.[41] Figure 4e shows measured R6G spectra from a nanogroove array (and flat Au surface) at $\lambda_0 = 785$ nm. Although the background spectrum is different, nine of the major R6G modes are shown, which demonstrates Raman activity of the nanogroove surfaces with similar measured intensities.

For low sample concentrations ($<10^{-6}$ M) the measurements are consistent with the population averaging effect.[4,5] For R6G sample concentrations ranging from 10^{-6} to 10^{-4} M (not all data shown), the measured spectra are very consistent and repeatable with respect to location and time. The enhancement factor has been estimated by comparing the peak heights of vibration spectra on the nanopyramid array surfaces with peak heights from reference measurements in solution while maintaining the same laser power, microscope system, spectrometer configuration, and R6G sample. A larger R6G concentration is used for the normal Raman reference measurement. The resulting areal average enhancement factor can be roughly estimated as $EF \approx S_{SERS}[C_R](S_R[C_{SERS}])^{-1}$, where S_{SERS} and $[C_{SERS}]$ are the intensity amplitude and R6G concentration from the SERS substrate, respectively, and S_R and $[C_R]$ are the intensity amplitude and R6G concentration from the normal Raman reference measurement. Due to the preresonance activity of R6G and low required laser power, enhancement factors at all measured vibration modes was not possible; however, an average $EF \approx 10^6$ has been measured for the $\nu = 1310$ cm^{-1} mode and we consider this to be a lower bound for the Raman scattering enhancement.

Conclusion

In summary, large area nanotextured surfaces with periodically self-aligned subwavelength nanogroove and nanopyramid array surfaces with precisely defined pitch λ_g and closely spaced adjacent nanostructures that form high-density arrays of hot-spot scattering sites ideal for SERS have been realized. The simple top-down fabrication technique requires a single lithography step and self-aligned wet anisotropic etching. Measured average Raman enhancement factors in deionized H_2O of $G \approx 10^6$ for R6G on Au surfaces with $\lambda_g = 200$ nm. The nanostructures can be scaled to smaller dimensions that will result in larger G as well as larger spatial density. The SERS-active substrates presented here represent an important step forward in precisely forming high-density arrays of hot-spot scattering sites with large field enhancements and reproducibility, which can be easily integrated with miniaturized lab-on-a-chip systems capable of analyzing nanoliter-scale sample volumes.

Acknowledgment. The authors thank Johan Bomer for device processing assistance, the MESA$^+$ cleanroom staff, Mark Smithers for assistance with HRSEM imaging, and Rico Keim for TEM sample preparation and imaging. This work was funded by the MEMSLand project within the Pointe-One program from The Netherlands Ministry of Economic Affairs.

References and Notes

(1) Fleischmann, M.; Hendra, P. J.; McQuillan, A. J. *Chem. Phys. Lett.* **1974**, *26*, 163.
(2) Moskovitz, M. *J. Chem. Phys.* **1978**, *69*, 4159.
(3) Jeanmaire, D. L.; Van Duyne, R. P. *J. Electroanal. Chem.* **1977**, *84*, 1.
(4) Hildebrandt, P.; Stockburger, M. *J. Phys. Chem.* **1984**, *88*, 5935.
(5) Nie, S.; Emory, S. R. *Science* **1997**, *275*, 1102.
(6) Kneipp, K.; Wang, Y.; Kneipp, H.; Perelman, L. T.; Itzkan, I.; Dasari, R.; Feld, M. S. *Phys. Rev. Lett.* **1997**, *78*, 1667.
(7) Michaels, A. M.; Nirmal, M.; Brus, L. E. *J. Am. Chem. Soc.* **1999**, *121*, 9932.
(8) Dieringer, J. A.; Wustholz, K. L.; Masiello, D. J.; Camden, J. P.; Kleinman, S. L.; Schatz, G. C.; Van Duyne, R. P. *J. Am. Chem. Soc.* **2009**, *131*, 849.
(9) Otto, A. *Top. Appl. Phys.* **1984**, *54*, 289.
(10) Moskovitz, M. *J. Raman Spectrosc.* **2005**, *36*, 485.
(11) Link, S.; El-Sayed, M. A. *J. Phys. Chem. B* **1999**, *103*, 8410.
(12) Wang, H.; Brandl, D. W.; Le, F.; Nordlander, P.; Halas, N. J. *Nano Lett.* **2006**, *6*, 827.
(13) Lu, Y.; Liu, G. L.; Kim, J.; Mejia, Y. X.; Lee, L. P. *Nano Lett.* **2005**, *5*, 119.
(14) McLellan, J. M.; Li, Z.-L.; Siekkinen, A. R.; Xia, Y. *Nano Lett.* **2007**, *7*, 1013.
(15) Rodríguez-Lorenzo, L.; Álvarez-Puebla, R. A.; Pastoriza-Santos, I.; Mazzucco, S.; Stéphan, O.; Kociak, M.; Liz-Marzán, L. M.; García de Abajo, F. J. *J. Am. Chem. Soc.* **2009**, *131*, 4616.
(16) Jackson, J. B.; Halas, N. J. *Proc. Natl. Acad. Sci. U.S.A.* **2004**, *101*, 17930.
(17) Inoue, M.; Ohtaka, K. *J. Phys. Soc. Jpn.* **1983**, *52*, 3853.
(18) Coyle, S.; Netti, C. M.; Baumberg, J. J.; Ghanem, M. A.; Birkin, P. R.; Bartlett, P. N.; Whittaker, D. M. *Phys. Rev. Lett.* **2001**, *87*, 176801.
(19) Shanmukh, S.; Jones, L.; Driskell, J.; Zhao, Y.; Dluhy, R.; Tripp, R. A. *Nano Lett.* **2006**, *6*, 2630.
(20) Masuda, H.; Fukuda, K. *Science* **1995**, *268*, 1466.
(21) Choi, D.; Choi, Y.; Hong, S.; Kang, T.; Lee, L. P. *Small* **2010**, *6*, 1741.
(22) Hulteen, J. C.; Van Duyne, R. P. *J. Vac. Sci. Technol., A* **1995**, *13*, 1553.
(23) Wu, L. Y.; Ross, B. M.; Lee, L. P. *Nano Lett.* **2009**, *9*, 1956.
(24) Bartlett, P. N.; Birkin, P. R.; Ghanem, M. A. *J. Chem. Soc., Chem. Commun.* **2000**, *17*, 1671.
(25) Kitson, S. C.; Barnes, W. L.; Sambles, J. R. *Phys. Rev. Lett.* **1999**, *77*, 2670.
(26) Gunnarsson, L.; Bjerneld, E. J.; Xu, H.; Petronis, S.; Kasemo, B.; Käll, M. *Appl. Phys. Lett.* **2001**, *78*, 802.
(27) Li, Z.; Tong, W. M.; Stickle, W. F.; Neiman, D. L.; Williams, R. S. *Langmuir* **2007**, *23*, 5135.
(28) Abu Hatab, N. A.; Oran, J. M.; Sepaniak, M. J. *ACS Nano* **2008**, *2*, 377.
(29) Brolo, A. G.; Arctander, E.; Gordon, R.; Leathem, B.; Kavanagh, K. L. *Nano Lett.* **2004**, *4*, 2015.
(30) Fromm, D. P.; Sundaramurthy, A.; Schuck, P. J.; Kino, G.; Moerner, W. E. *Nano Lett.* **2004**, *4*, 957.
(31) Porto, J. A.; Garcia-Vidal, F. J.; Pendry, J. B. *Phys. Rev. Lett.* **1999**, *83*, 2845.
(32) Perney, N. M. B.; Baumberg, J. J.; Zoorob, M. E.; Charlton, M. D. B.; Mahnkopf, S.; Netti, C. M. *Opt. Express* **2006**, *14*, 847.
(33) Gao, H.; Henzie, J.; Lee, M. H.; Odom, T. W. *Proc. Natl. Acad. Sci. U.S.A.* **2008**, *105*, 20146.
(34) Lin, T.-H.; Linn, N. C.; Tarajano, L.; Jiang, B.; Jiang, P. *J. Phys. Chem. C* **2009**, *113*, 1367.

(35) Wood, R. W. *Philos. Mag.* **1902**, *4*, 396.
(36) Tsang, J. C.; Kirtley, J. R.; Bradley, J. A. *Phys. Rev. Lett.* **1979**, *43*, 772.
(37) Girlando, A.; Philpott, M. R.; Heitmann, D.; Swalen, J. D.; Santo, R. *J. Chem. Phys.* **1980**, *72*, 5187.
(38) Weber, M.; Mills, D. L. *Phys. Rev. B* **1983**, *27*, 2698.
(39) Raether, H. *Surface Plasmons on Smooth and Rough Surfaces and on Gratings*; Springer: Berlin, Germany, 1988.
(40) Baltog, I.; Primeau, N.; Reinisch, R. *Appl. Phys. Lett.* **1995**, *66*, 1187.
(41) García-Vidal, F. J.; Pendry, J. B. *Phys. Rev. Lett.* **1996**, *77*, 1163.
(42) Sobnack, M. B.; Tan, W. C.; Wanstall, N. P.; Preist, T. W.; Sambles, J. R. *Phys. Rev. Lett.* **1998**, *80*, 5667.
(43) Vernon, K. C.; Davis, T. J.; Scholes, F. H.; Gómez, D. E.; Lau, D. *J. Raman Spectrosc.* **2010**, *41*, 1106.
(44) Barnes, W. L.; Dereux, A.; Ebbesen, T. W. *Nature* **2003**, *424*, 824.
(45) Xuegong, D.; Braun, G. B.; Liu, S.; Sciortino, P. F., Jr.; Koefer, B.; Tombler, T.; Moskovits, M. *Nano Lett.* **2010**, *10*, 1780.
(46) Seidel, H.; Csepregi, L.; Heuberger, A.; Baumgartel, H. *J. Electrochem. Soc.* **1990**, *137*, 3612.
(47) Chen, S.; Bomer, J. G.; van der Wiel, W. G.; Carlen, E. T.; van den Berg, A. *ACS Nano* **2009**, *3*, 3485.
(48) Michaels, A. M.; Jiang, J.; Brus, L. *J. Phys. Chem. B* **2000**, *104*, 11965.
(49) Haes, A. J.; Chang, L.; Klein, W. L.; Van Duyne, R. P. *J. Am. Chem. Soc.* **2005**, *127*, 2264.
(50) Pully, V. V.; Lenferink, A.; Otto, C. *J. Raman Spectrosc.* **2009**, *41*, 599.
(51) Watanabe, H.; Hayazawa, N.; Inouye, Y.; Kawata, S. *J. Phys. Chem. B* **2005**, *109*, 5012.
(52) Jiang, J.; Bosnick, K.; Maillard, M.; Brus, L. *J. Phys. Chem. B* **2003**, *107*, 9964.

JP106245A